

Asymmetric response of interfacial water to applied electric fields

<https://doi.org/10.1038/s41586-021-03504-4>

Received: 8 June 2019

Accepted: 29 March 2021



Check for updates

Angelo Montenegro¹, Chayan Dutta¹, Muhammet Mammetkuliev¹, Haotian Shi², Bingya Hou², Dhritiman Bhattacharyya¹, Bofan Zhao², Stephen B. Cronin² & Alexander V. Benderskii^{1✉}

Our understanding of the dielectric response of interfacial water, which underlies the solvation properties and reaction rates at aqueous interfaces, relies on the linear response approximation: an external electric field induces a linearly proportional polarization. This implies antisymmetry with respect to the sign of the field. Atomistic simulations have suggested, however, that the polarization of interfacial water may deviate significantly from the linear response. Here we present an experimental study addressing this issue. We measured vibrational sum-frequency generation spectra of heavy water (D₂O) near a monolayer graphene electrode, to study its response to an external electric field under controlled electrochemical conditions. The spectra of the OD stretch show a pronounced asymmetry for positive versus negative electrode charge. At negative charge below 5×10^{12} electrons per square centimetre, a peak of the non-hydrogen-bonded OD groups pointing towards the graphene surface is observed at a frequency of 2,700 per centimetre. At neutral or positive electrode potentials, this ‘free-OD’ peak disappears abruptly, and the spectra display broad peaks of hydrogen-bonded OD species (at 2,300–2,650 per centimetre). Miller’s rule¹ connects the vibrational sum-frequency generation response to the dielectric constant. The observed deviation from the linear response for electric fields of about $\pm 3 \times 10^8$ volts per metre calls into question the validity of treating interfacial water as a simple dielectric medium.

Liquid water owes most of its physical and chemical properties to the dynamical network of hydrogen bonds. The network represents a subtle interplay between local interactions reflecting the geometry of the water molecules (the charge distribution and polarizability of the OH bonds and lone pairs), and the long-range electrostatic (dipole–dipole) interactions. This interplay underlies the complexity of water’s response to an electric field. The molecular-level picture of this response is essential to our understanding of its properties as a dielectric medium² (in the case of an externally applied electric field) and as a polar solvent (in the case of the electric field around a solute molecule)³. Application of an external electric field via a planar electrode is therefore a useful tool for studying the hydrogen-bond network of water, by quantifying the magnitude of the response relative to the strength of the perturbation. A simplistic picture is partial alignment of the water dipoles by the electric field, a result of competition between the torque produced on a given molecule by the field–dipole interaction and the hydrogen bonds between this molecule and its neighbours, which, in the absence of the field, yield the isotropic orientational distribution in bulk water.

Vibrational spectroscopy of water is a natural match for studying aqueous hydrogen bonds, mostly owing to the well-researched relationship between the frequency shifts of the OH- or OD-stretch modes and the local hydrogen-bonding environment^{4–6}. Surface-selective vibrational sum-frequency generation (VSFG) spectroscopy has been applied to study

the molecular structure of water at charged interfaces such as mineral surfaces (where the surface charge can be adjusted by varying the pH of the solution)^{7,8} or monolayers of surfactants with charged headgroups^{9,10}.

The asymmetry of the interfacial environment makes aqueous hydrogen bonds at interfaces different from bulk water. We can classify the factors underlying the interfacial asymmetry into three categories: (1) geometric termination of the 3D network of hydrogen bonds at the interface, which may be planar or have nanometre- or molecular-scale morphology (for example, capillary waves, corrugated/nanostructured surfaces, and/or shape and spatial arrangement of the surfactant headgroups); (2) surface electrostatics—effects of the surface charge and the spatial distributions of counterions (if any) in the water phase; and (3) specific local interactions of interfacial water molecules with the molecules (for example, hydrophilic versus hydrophobic) of the other phase. The electrostatic effects (type 2) due to the field of a planar charged surface would be generally applicable to all charged interfaces. It would therefore be useful to disentangle these from other types of interaction. However, this is difficult for the systems studied previously, where all three factors are simultaneously present: for example, hydrogen bonding of water to the hydrophilic surfactant headgroups or hydroxyl moieties on a mineral surface. The situation is further complicated by the morphology of the surface (especially in the case of surfactant monolayers) and the presence of counterions, whose spatial distribution affects the local electric fields.

¹Department of Chemistry, University of Southern California, Los Angeles, CA, USA. ²Department of Electrical Engineering, University of Southern California, Los Angeles, CA, USA.

✉e-mail: alex.benderskii@usc.edu

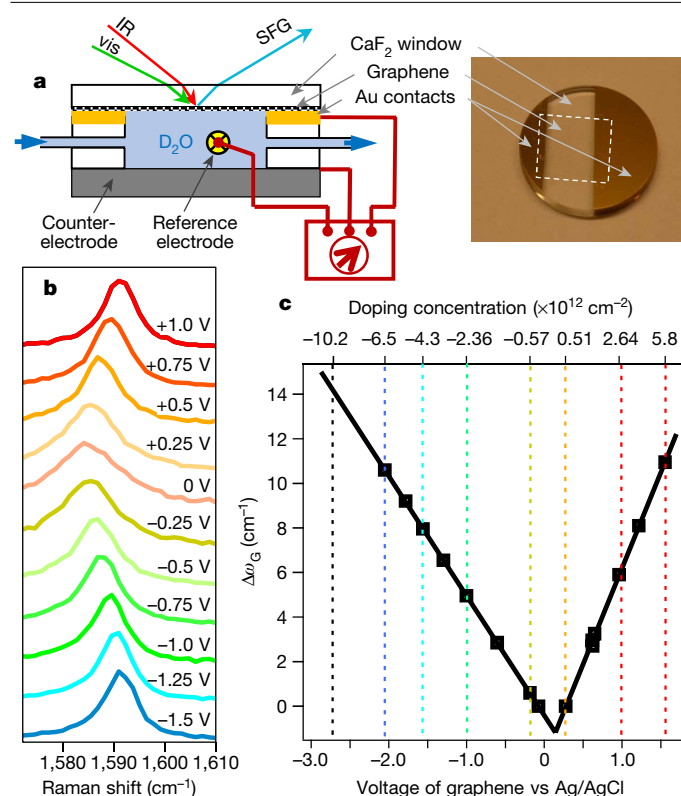


Fig. 1 | Experimental cell and graphene doping concentration measurements. **a**, Schematic diagram of the experimental electrochemical flow cell with a monolayer graphene electrode and gold contact strips supported on a CaF_2 window. The counter-electrode is glassy carbon, and the reference electrode is Ag/AgCl . **b**, Raman spectra of the G-band of graphene electrode, recorded as a function of electrochemical potential (versus Ag/AgCl). The spectra are vertically offset for clarity. **c**, The G-band central frequency versus electrode potential. Squares, experimental points; solid lines, linear fit. The vertical grid lines and the top axis indicate the potentials at which the VSFG spectra were recorded and the corresponding doping concentrations of the graphene electrode.

Our approach uses a monolayer graphene electrode to apply charge to interfacial water, the response of which is then measured via in situ VSFG spectroscopy under controlled electrochemical conditions. Monolayer graphene is atomically flat, conductive, chemically inert and nearly transparent (2.3% absorbance) throughout the visible and infrared spectral ranges¹¹. This system enables us to continuously vary the surface charge from negative to positive without altering the chemical composition of the surface. Our experimental cell is schematically depicted in Fig. 1a and described in detail in the Methods.

The frequency shift of the G-band Raman mode of monolayer graphene (Fig. 1b) provides an intrinsic measure of the excess charge density via a well-established relationship (see Methods). Graphene's G-band frequency reaches a minimum at the charge-neutral point around +0.1 V versus Ag/AgCl and blueshifts linearly as a function of the applied potential (Fig. 1c).

Voltage-dependent VSFG spectra of D_2O at the graphene interface (Fig. 2) were collected using the SSP polarization combination (where S is electric-field polarization perpendicular to the plane of incidence and P is electric-field polarization parallel to the plane of incidence) for the sum-frequency generation (SFG), visible and infrared beams, respectively. Applying a negative (positive) bias dopes the graphene with electrons (holes), yielding negatively (positively) charged interfaces (Fig. 1c). The asymmetry in the observed spectra with respect to positive versus negative applied fields is striking. At -1.6 V (versus

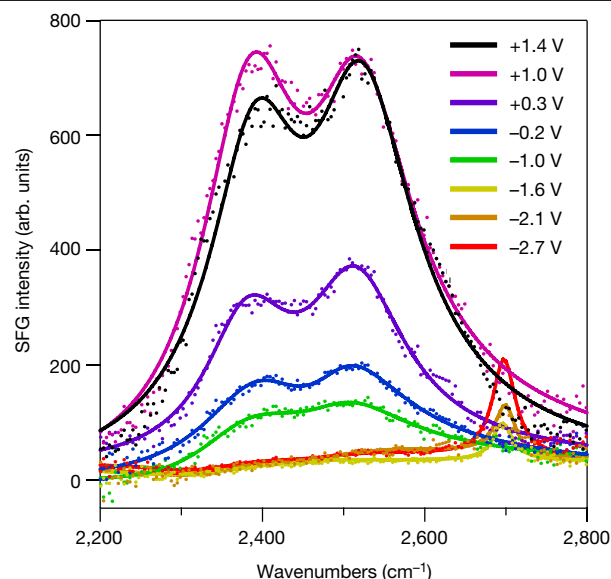


Fig. 2 | VSFG spectra of D_2O at the graphene electrode, at different electrode potentials versus Ag/AgCl . The spectra in the OD-stretch spectral region were recorded using the SSP polarization combination (infrared, visible, SFG). Solid lines show the fit to the model with interfering surface and bulk contributions described in equation (3). The potentials are converted to surface charge densities according to Fig. 1c.

Ag/AgCl) and below, the VSFG spectra of the graphene– D_2O interface exhibits one relatively narrow peak (full-width at half-maximum, $\text{FWHM} \approx 30 \text{ cm}^{-1}$) at $2,697 \pm 3 \text{ cm}^{-1}$ (Fig. 2). We assign this feature to the free-OD stretch, a local mode of water in the topmost monolayer, where one OD group points away from the bulk, towards the graphene surface, and into a vacuum gap of about 3 Å (suggested by molecular dynamics studies)^{12,13}. It is therefore unable to form a hydrogen bond with other water molecules, and is blueshifted and narrow relative to the broad peaks of the hydrogen-bonded species, similar to the air–water interface^{14,15}. It should be noted that, although liquid bulk water has a fraction of broken hydrogen bonds, the free-OD peak is absent in the spectrum of bulk water, and only the surface species contribute to that peak. Additionally, the free-OD species is absent in the spectra of other, previously studied charged interfaces^{7–10}, where the free-OD signal is suppressed because of hydrogen-bonding interactions with those surfaces. For voltages of -1.0 V and above, the free-OD feature is absent and only broad hydrogen-bonded peaks are observed in the $2,300 \text{ cm}^{-1}$ to $2,650 \text{ cm}^{-1}$ region^{6,16}. Near the charge-neutral point, the free-OD feature is absent, consistent with the experimental work of Singla et al.¹⁷, who measured VSFG spectra of H_2O in contact with graphene surface in an open-circuit configuration. However, this observation contradicts theoretical studies of the graphene–water interface, which predict the presence of a free-OD feature at the neutral potential¹².

As indicated in Fig. 1c, the range of applied potentials corresponds to the surface charge densities σ on the graphene electrode from $-1.0 \times 10^{13} \text{ cm}^{-2}$ to $+5.0 \times 10^{12} \text{ cm}^{-2}$. Taking into account the vacuum gap between the graphene and water, we can estimate an upper limit of the electric field experienced by the topmost layers of water at the electrode surface as that of an infinitely charged plane: $E_0(0) = \sigma / (2\epsilon_0\epsilon)$ (with $\epsilon = 1$), giving a maximum electric field of -0.092 V Å^{-1} . The field is expected to be weaker for deeper layers of water.

Although VSFG ($\omega_{\text{SFG}} = \omega_1 + \omega_2$) is nominally a second-order nonlinear optical process, the static electric field ($E_0, \omega_3 = 0$) at a charged interface results in a third-order contribution to the signal:

$$E_{\text{SFG}} = \chi^{(2)} : E_{\omega_1} E_{\omega_2} + \chi^{(3)} : E_{\omega_1} E_{\omega_2} E_0 \quad (1)$$

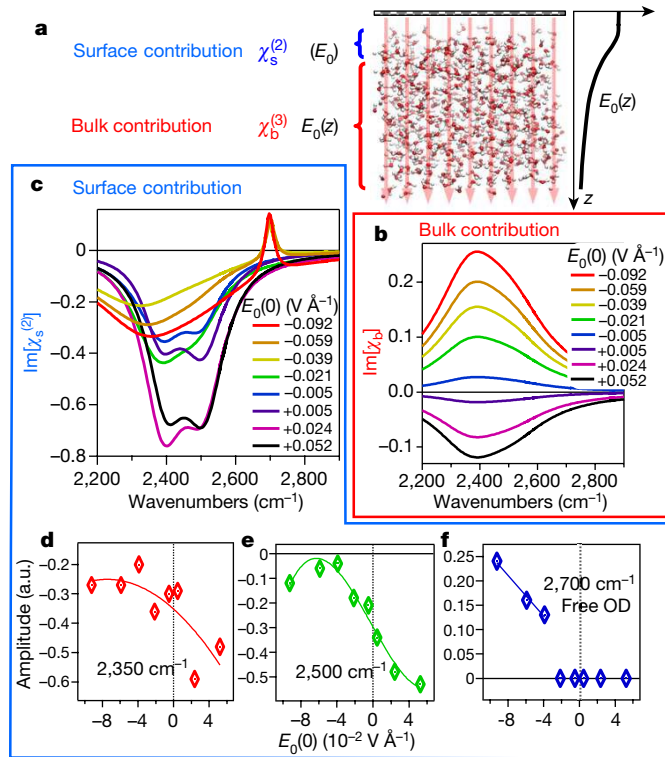


Fig. 3 | Disentangling the surface response of water from the bulk response. **a**, Schematic illustration of the spatial separation of the surface and bulk contributions to the VSFG signal at the water–graphene electrode interface, and the depth dependence of the applied electric field $E_0(z)$. **b**, As shown by previous studies, the bulk contribution $X_b(E_0)$ resembles the bulk water absorption spectrum and behaves as expected according to the linear response approximation: charge reversal results in the sign reversal of the response. **c**, The extracted surface contribution $\chi_s^{(2)}(E_0)$ as a function of the applied field (plotted here is its imaginary part) shows pronounced deviations from the linear response behaviour. **d–f**, Spectral amplitudes of the three Lorentzian peaks used to fit the surface contribution (**c**), as a function of the applied field. **d**, **e**, The amplitudes of the peaks centred at 2,350 cm^{-1} and 2,500 cm^{-1} , respectively, corresponding to the hydrogen-bonded water species. Solid lines show a fourth-order polynomial fit. **f**, The amplitude of the free-OD peak centred at 2,700 cm^{-1} ; as evident from the raw spectra (Fig. 2), this peak is absent at fields $\geq -0.02 \text{ V } \text{\AA}^{-1}$.

It is generally accepted that the $\chi_s^{(2)}$ contribution originates from a few topmost monolayers of water^{10,15,18} (beyond which the isotropic orientational distribution of bulk water is restored, resulting in zero SFG signal). In contrast, the region contributing to the $\chi_s^{(3)}$ signal may extend into the liquid as far as the static field $E_0(z)$ penetrates; this field decays over the Debye screening length^{18,19}. Inspired by ref.¹⁰, we spatially separate the $\chi_s^{(3)}$ contribution into the ‘surface’ part, originating from the same interfacial region as $\chi_s^{(2)}$, and a ‘bulk’ part (Fig. 3a). The surface contribution $\chi_s^{(3)}$ can be thought of as the change in the interfacial second-order susceptibility due to the static field $E_0(0)$ estimated above:

$$\chi_s^{(2)}(E_0) = \chi_s^{(2)}(0) + \chi_s^{(3)} E_0 \quad (2)$$

The bulk contribution $\chi_b^{(3)}$ is integrated over the depth (z), which results in the celebrated Eisenthal relationship of the surface potential $\Phi(0)$ (ref.²⁰). When the Debye screening length is comparable to the wavelength of light, phase-retardation effects become important in the interference of the bulk $\chi_b^{(3)}$ contribution and

the surface signal¹⁰, for which a formal expression was recently derived^{18,19}:

$$I_{\text{SFG}} \propto \left| \chi_s^{(2)}(E_0) + \frac{\kappa e^{i\varphi}}{\sqrt{\kappa^2 + (\Delta k_z)^2}} \chi_b^{(3)} \Phi_0(0) \right|^2, \quad \varphi = \arctan \frac{\Delta k_z}{\kappa} \quad (3)$$

where κ is the inverse of the Debye screening length and $\Delta k_z = k_{\text{SFG},z} - k_{1,z} - k_{2,z}$ is the inverse of the coherence length of the SFG process. In our case of pure D_2O (no electrolyte added), the Debye length is of the order of 1 μm .

Recent studies of several charged aqueous interfaces (various lipid monolayers and mineral surfaces) have concluded that the bulk contribution—the second term in equation (3), which we denote $X_b(E_0) = \frac{\kappa e^{i\varphi}}{\sqrt{\kappa^2 + (\Delta k_z)^2}} \chi_b^{(3)} \Phi_0(0)$ —has nearly the same spectral lineshape regardless of the chemical nature of the surface, and follows the linear response: that is, it is proportional to the static field (and the potential) of the surface^{12,20,21}. We used this spectral shape of the bulk contribution^{10,16,18} in fitting our VSFG spectra to equation (3), allowing us to extract the spectra of the interfacial water as a function of the surface field $\chi_s^{(2)}(E_0)$.

The results of the spectral decomposition are presented in Fig. 3b,c, where the imaginary parts of the bulk and surface contributions are shown. Consistent with the previous studies in both shape and sign, the assumed bulk contribution $\text{Im}[X_b]$, represented by two broad Lorentzians at 2,365 cm^{-1} and 2,510 cm^{-1} (FWHM = 150 cm^{-1}), resembles the linear absorption spectrum of bulk water and scales linearly with the applied field $E_0(0)$.

The extracted surface contribution $\chi_s^{(2)}(E_0)$ does not follow the linear response behaviour, showing a pronounced asymmetry with respect to positive versus negative surface charge. We fit the $\chi_s^{(2)}(E_0)$ spectra with three Lorentzians: one narrow peak at 2,697 cm^{-1} representing the free-OD species, and two broader redshifted peaks at 2,350 cm^{-1} and 2,500 cm^{-1} representing hydrogen-bonded structures. The amplitudes of these spectral components as a function of the applied field are shown in Fig. 3d–f. The nonlinearity implies that the surface signal does not behave according to equation (2). Note that although our VSFG measurements were performed at the intensity level, the signs of the extracted spectral components are consistent with all previous studies that used optical heterodyne detection^{9,10,15}. If we define the sign of $\text{Im}[\chi^{(2)}]$ for the free-OD feature as positive (free-OD groups always point up), then the bulk contribution $\text{Im}[X_b]$ is positive at negatively charged surfaces and negative at positively charged surfaces. For negative fields, the sign of the hydrogen-bonded part of the surface contribution also is negative.

The well-established Miller’s rule in nonlinear optics¹ is a proportionality relationship between a nonlinear susceptibility and a product of the first-order (linear) susceptibilities at constituent frequencies. It works well for off-resonant responses and therefore for d.c. fields, as was pointed out in Miller’s original paper¹. A straightforward extension of Miller’s rule to our case suggests that the change of the second-order susceptibility in response to the static field of a charged surface, equation (2), is proportional to the linear d.c. susceptibility of the interfacial layer,

$$\chi_s^{(3)}(\omega_1, \omega_2, 0) = \chi_s^{(2)}(\omega_1, \omega_2) \chi_s^{(1)}(0) \quad (4)$$

(Note that we only consider the off-resonant zero-frequency component for the proportionality relationship; the proportionality does not imply that the second-order susceptibility $\chi_s^{(2)}(\omega_1, \omega_2)$ is related to the residual spectrum at zero field, $\chi_s^{(2)}(0)$ in equation (2).) The linear susceptibility is connected to the dielectric constant of the interfacial layer, $\epsilon_s = 1 + 4\pi\chi_s^{(1)}(0)$. Thus, our experimental demonstration that interfacial water responds nonlinearly to applied electric fields suggests that the assumption of a linear dielectric response in attempts

to better understand the behaviour of this surface layer may be invalid. The deviation of the electrostatics of interfacial water from the linear response behaviour has been well established by multiple theoretical and computer simulation studies and has important consequences for practical applications^{21–25}. Recent studies of nanoconfined water have also shown anomalous behaviour of the dielectric response effected by surface interactions²⁶.

At the surface charge densities explored in our study (from $-1.0 \times 10^{13} \text{ e}^- \text{ cm}^{-2}$ to $+5.0 \times 10^{12} \text{ e}^- \text{ cm}^{-2}$, that is, -0.016 C m^{-2} to $+0.008 \text{ C m}^{-2}$), the electric field strengths are of the order of $\pm 0.03 \text{ V \AA}^{-1}$ at the interface and decay into the bulk. Dielectric saturation in bulk water manifests itself as a simple monotonic decrease of the effective dielectric constant (defined as a derivative of the induced polarization versus applied static electric field), which begins to deviate from the $\epsilon \approx 80$ value at electric fields of the order of 10^9 V m^{-1} (0.1 V \AA^{-1})²⁷. The bulk contribution $X_b(E_0)$ obeys the linear behaviour, consistent with this limit, as deeper water layers experience a weaker static field than at the interface, well below the dielectric saturation limit. However, the response of interfacial water deviates from linear behaviour at much weaker fields and in a non-monotonic fashion. We also note that the average surface charge density in many commonly occurring systems, such as phospholipid monolayers and bilayers, can be as high as one elementary charge per 60 \AA^2 , whereas here it is less than one elementary charge per $1,000 \text{ \AA}^2$. Additionally, the local fields are expected to be even stronger around discrete charged headgroups. The order of magnitude of the dielectric saturation field in liquid water, $\sim 10^9 \text{ V m}^{-1}$, can be qualitatively understood as being comparable to the field imposed by the nearest neighbour molecules. From this standpoint, it makes sense that interfacial water should tend to exhibit nonlinear effects at weaker fields, owing to the smaller average number of nearest neighbours.

It is interesting to consider possible molecular mechanisms responsible for the nonlinear behaviour of interfacial water^{21,25,28}, in contrast with bulk water. Water polarization is largely due to reorientation of the molecular dipoles. Evolution of the VSFG spectra as a function of the applied field offers insight into the molecular orientation and rearrangement of hydrogen bonds. One obvious clue is the disappearance of the free-OD feature at neutral or positive potentials. At a negatively charged interface (applied potentials below -1 V versus Ag/AgCl), the free-OD signal abruptly appears as a narrow blueshifted peak in the VSFG spectra, indicating that the free-OD moiety probably points towards the graphene, into the vacuum gap. As the surface becomes neutral or positive, the free-OD species orient away from graphene and towards bulk water, where they are more likely to find hydrogen-bonding partners and no longer contribute to the free-OD peak. This suggests a sudden rearrangement of the structure of the interfacial layer. Such an asymmetric response may be one of the mechanisms of the linear response breakdown. Recent surface-enhanced Raman experiments have been interpreted in this way²⁹. Molecular reorientation and interconversion between different hydrogen-bonding classes leading to large-scale structural rearrangement of the surface layer can be viewed as a field-induced phase transition of interfacial water, which was first suggested based on temperature-jump relaxation measurements in the 1980s³⁰. We hope that our work will stimulate further theoretical and experimental studies of the molecular mechanisms underpinning the unusual behaviour of interfacial water.

Online content

Any methods, additional references, Nature Research reporting summaries, source data, extended data, supplementary information,

acknowledgements, peer review information; details of author contributions and competing interests; and statements of data and code availability are available at <https://doi.org/10.1038/s41586-021-03504-4>.

1. Miller, R. C. Optical second harmonic generation in piezoelectric crystals. *Appl. Phys. Lett.* **5**, 17–19 (1964).
2. Wyman, J. Measurements of the dielectric constants of conducting media. *Phys. Rev.* **35**, 623–634 (1930).
3. Kirkwood, J. G. The dielectric polarization of polar liquids. *J. Chem. Phys.* **7**, 911–919 (1939).
4. Fecko, C. J., Eaves, J. D., Loparo, J. J., Tokmakoff, A. & Geissler, P. L. Ultrafast hydrogen-bond dynamics in the infrared spectroscopy of water. *Science* **301**, 1698–1702 (2003).
5. Bakker, H. J. & Skinner, J. L. Vibrational spectroscopy as a probe of structure and dynamics in liquid water. *Chem. Rev.* **110**, 1498–1517 (2010).
6. Nihonyanagi, S. et al. Unified molecular view of the air/water interface based on experimental and theoretical $\chi^{(2)}$ spectra of an isotopically diluted water surface. *J. Am. Chem. Soc.* **133**, 16875–16880 (2011).
7. Du, Q., Freysz, E. & Shen, Y. R. Vibrational spectra of water molecules at quartz/water interfaces. *Phys. Rev. Lett.* **72**, 238–241 (1994).
8. Schaefer, J., Gonella, G., Bonn, M. & Backus, E. H. G. Surface-specific vibrational spectroscopy of the water/silica interface: screening and interference. *Phys. Chem. Chem. Phys.* **19**, 16875–16880 (2017).
9. Nihonyanagi, S., Yamaguchi, S. & Tahara, T. Direct evidence for orientational flip-flop of water molecules at charged interfaces: a heterodyne-detected vibrational sum frequency generation study. *J. Chem. Phys.* **130**, 204704 (2009).
10. Wen, Y. C. et al. Unveiling microscopic structures of charged water interfaces by surface-specific vibrational spectroscopy. *Phys. Rev. Lett.* **116**, 016101 (2016).
11. Nair, R. R. et al. Fine structure constant defines visual transparency of graphene. *Science* **320**, 1308 (2008).
12. Ohto, T., Tada, H. & Nagata, Y. Structure and dynamics of water at water-graphene and water-hexagonal boron-nitride sheet interfaces revealed by ab initio sum-frequency generation spectroscopy. *Phys. Chem. Chem. Phys.* **20**, 12979–12985 (2018).
13. Ostrowski, J. H. J. & Eaves, J. D. The tunable hydrophobic effect on electrically doped graphene. *J. Phys. Chem. B* **118**, 530–536 (2014).
14. Du, Q., Superfine, R., Freysz, E. & Shen, Y. R. Vibrational spectroscopy of water at the vapor/water interface. *Phys. Rev. Lett.* **70**, 2313–2316 (1993).
15. Stiopkin, I. V. et al. Hydrogen bonding at the water surface revealed by isotopic dilution spectroscopy. *Nature* **474**, 192–195 (2011).
16. Ohno, P. E., Wang, H.-f., Paesani, F., Skinner, J. L. & Geiger, F. M. Second-order vibrational line-shapes from the air/water interface. *J. Phys. Chem. A* **122**, 4457–4464 (2018).
17. Singla, S. et al. Insight on structure of water and ice next to graphene using surface-sensitive spectroscopy. *ACS Nano* **11**, 4899–4906 (2017).
18. Ohno, P. E., Wang, H.-f. & Geiger, F. M. Second-order spectral line shapes from charged interfaces. *Nat. Commun.* **8**, 1032 (2017).
19. Gonella, G., Lütgebaucks, C., de Beer, A. G. F. & Roke, S. Second harmonic and sum-frequency generation from aqueous interfaces is modulated by interference. *J. Phys. Chem. C* **120**, 9165–9173 (2016).
20. Ong, S., Zhao, X. & Eisenthal, K. B. Polarization of water molecules at a charged interface: second harmonic studies of the silica/water interface. *Chem. Phys. Lett.* **191**, 327–335 (1992).
21. Zhang, Y., de Aguiar, H. B., Hynes, J. T. & Laage, D. Water structure, dynamics, and sum-frequency generation spectra at electrified graphene interfaces. *J. Phys. Chem. Lett.* **11**, 624–631 (2020).
22. Bratko, D., Daub, C. D., Leung, K. & Luzar, A. Effect of field direction on electrowetting in a nanopore. *J. Am. Chem. Soc.* **129**, 2504–2510 (2007).
23. von Domaros, M., Bratko, D., Kirchner, B. & Luzar, A. Dynamics at a Janus interface. *J. Phys. Chem. C* **117**, 4561–4567 (2013).
24. Na, X., Ning, Z. & Rong-Qing, X. Effect of driving voltage polarity on dynamic response characteristics of electrowetting liquid lens. *Jpn. J. Appl. Phys.* **57**, 052201 (2018).
25. Zhang, Y., Stirnemann, G., Hynes, J. T. & Laage, D. Water dynamics at electrified graphene interfaces: a jump model perspective. *Phys. Chem. Chem. Phys.* **22**, 10581–10591 (2020).
26. Fumagalli, L. et al. Anomalous low dielectric constant of confined water. *Science* **360**, 1339 (2018).
27. Alper, H. E. & Levy, R. M. Field strength dependence of dielectric saturation in liquid water. *J. Phys. Chem.* **94**, 8401–8403 (1990).
28. Zhang, C. & Sprik, M. Electromechanics of the liquid water vapour interface. *Phys. Chem. Chem. Phys.* **22**, 10676–10686 (2020).
29. Li, C.-Y. et al. In situ probing electrified interfacial water structures at atomically flat surfaces. *Nat. Mater.* **18**, 697–701 (2019).
30. Benderskii, V. A. & Velichko, G. I. Temperature jump in electric double-layer study: Part I. Method of measurements. *J. Electroanal. Chem. Interfacial Electrochem.* **140**, 1–22 (1982).

Publisher's note Springer Nature remains neutral with regard to jurisdictional claims in published maps and institutional affiliations.

© The Author(s), under exclusive licence to Springer Nature Limited 2021

Methods

Sample preparation

Prior to transferring the graphene, two gold strips (50 nm thick) were deposited onto a transparent CaF_2 window (25.4 mm diameter \times 1 mm thickness, OptoCity Inc.) by electron-beam evaporation using a shadow mask. Monolayer graphene was grown by chemical vapour deposition on copper foil at 1,000 °C in methane and H_2 gas at a reduced pressure of 1–1.5 torr (ref. ³¹). After growth, the copper foil was spin-coated with polymethyl methacrylate (PMMA-A6) at 2,000 rpm for 45 s and then baked at 150 °C for 5 min. The copper foil was etched away, and the graphene (1 cm \times 1.5 cm) with PMMA was scooped out, rinsed with 10% HCl and DI water, and transferred to the CaF_2 window³². To improve adhesion, the sample was baked at 120 °C for 5 min (ref. ³³). The residual PMMA layer was removed by placing the sample in an acetone bath for 5 min, followed by a rinse with isopropyl alcohol and then DI water. The gold strips provide macroscopic contacts through which we measure the resistance across the graphene electrode (typically 1–2 k Ω) and apply voltage. The sample is shown in Fig. 1a.

Electrochemical cell

Our experimental cell is schematically depicted in Fig. 1a. The monolayer graphene electrode is supported on a CaF_2 substrate, which forms the top window of the electrochemical flow-cell, with graphene facing the water (D_2O). A glassy carbon counter-electrode forms the bottom of the sandwich-type flow-cell, held together by friction between two circular aluminium plates. The separation between the top and bottom electrodes is held by an 8-mm-thick cylindrical Teflon spacer (Fig. 1a, left panel). The top aluminium plate has an opening of about 0.8" in diameter, which permits light to pass into and out of the cell. D_2O (Cambridge Isotopes Laboratories Inc., 99.9% purity) was continually cycled through the input and output ports of the Teflon spacer via a peristaltic pump (Fisher Scientific, model 13-876-2) to reduce laser-induced heating of the sample. No electrolyte was added to D_2O in our experiments. The Teflon spacer was cleaned with piranha solution, a 3:1 (by volume) concentrated sulfuric acid to 30% H_2O_2 . In the two-terminal configuration, the graphene and glassy carbon electrodes were connected to the positive and negative terminals of a voltage source (Keithley Instruments, model 2400), respectively. In the three-terminal configuration, the graphene, glassy carbon and Ag/AgCl electrodes served as the working, counter- and reference electrodes respectively, and were connected to a potentiostat (Gamry Instruments, Reference 600). The reference electrode was inserted through the side wall of the Teflon spacer, immersed in D_2O between the working and counter-electrodes. The in-plane resistance of the monolayer graphene (typically 1–2 k Ω) was monitored between two evaporated gold electrodes (Fig. 1a, right panel) to ensure that no degradation of the graphene monolayer occurred during the course of the measurements.

Spectro-electrochemical methods

VSFG spectra of the graphene–water interface in the SSP polarization configuration (referring to the polarization of the SFG, visible and infrared beams respectively) were acquired at each applied voltage in the two-terminal cell configuration. The incoming visible and infrared laser beams access the graphene–water interface through the CaF_2 window of the sample, and the VSFG signal generated in the reflection direction exits the cell through the same window. We used the broadband VSFG technique, which combines a femtosecond mid-infrared pulse centred at the OD-stretch band, 2,500 cm^{-1} (FWHM = 375 cm^{-1}) with a narrowband (picosecond) visible pulse at 806 nm (\sim 2 ps, FWHM = 10 cm^{-1})³⁴. An equilibration time of 2 min was allowed to elapse at each voltage to ensure that the measurements were performed in the steady state. Applying potentials that exceeded a safe range of approximately -3 V to 1.8 V (versus Ag/AgCl) tended to diminish the reproducibility of subsequent spectroscopic measurements. We correlated the decline in reproducibility with a jump

in the resistance across the graphene electrode by threefold or more. At that point, the 2*D*- to *G*-band intensity ratio of the graphene was no longer 2:1 (Extended Data Fig. 1), and a pronounced *D*-band (\sim 1,345 cm^{-1}) peak appeared in the Raman spectra, indicating that the graphene was no longer defect-free³⁵. Although some of the applied voltages lie outside the range of electrochemical stability of water, graphene is an inert electrode and the rate of the water splitting is slow, as indicated by the relatively small electrochemical current flowing through the cell—below 100 μA at -2.7 V for the graphene electrode area of 1.5 cm^2 . At this level of current, one electron is transferred per area occupied by a single water molecule (\sim 10 \AA^2) every 2 s, on average. In contrast, the timescale of the spectroscopic measurement is shorter than 1 ps (vibrational dephasing time of the OD-stretch modes). The electrochemical current was linearly proportional to the applied voltage within the safe range of operation (Extended Data Fig. 2). The applied voltages for each spectral acquisition were randomly staggered (instead of stepping the voltage in a single direction) to rule out any effects associated with irreversible changes to the electrode, and the 0.3-V spectrum was periodically re-measured to ensure that there was no drift in the signal over time (Extended Data Fig. 3). We found no evidence of water trapped between the graphene and CaF_2 substrate, as an empty ('dry') cell yielded no VSFG signal. The VSFG signal in the D_2O region vanished on isotopic dilution with H_2O , confirming that the signal originated from D_2O (Extended Data Fig. 4). To discourage the dissolution of atmospheric H_2O and CO_2 into the D_2O , the reservoir was sealed and kept in an environment purged of CO_2 and water during experiments.

We opted to carry out the VSFG experiments in the two-terminal configuration because the electrochemical currents were lower when the reference electrode was absent. The voltage applied to graphene in the two-terminal configuration (versus a glassy carbon counter-electrode) was converted to a three-terminal voltage (versus an Ag/AgCl reference electrode) so that the applied voltages in the two-terminal configuration could be reported without the effect of voltage drops across the D_2O at the graphene and glassy carbon interfaces and with respect to a standard reference potential. The conversion was achieved via Raman spectroscopic measurements of graphene's *G*-band, which shifted linearly with respect to the applied voltage in both two-terminal and three-terminal configurations (Extended Data Fig. 5). Given a two-terminal voltage, the corresponding three-terminal voltage is that which yields the same *G*-band shift.

The frequency shift of the *G*-band Raman mode of monolayer graphene provides an intrinsic measure of the excess charge density via a well-established relationship. In situ Raman spectra of the graphene electrode were collected under applied electrochemical potentials. The *G*-band frequency of the graphene, around 1,585 cm^{-1} , reaches a minimum at the charge neutral point around +0.1 V versus Ag/AgCl. The *G*-band Raman frequency blueshifts linearly as a function of the applied potential, as plotted in Fig. 1b,c. From the *G*-band frequency shift $\Delta\omega_G$, the Fermi energy E_F and doping concentration n (Fig. 1c) were calculated through the following relations in the literature^{36,37}:

$$\text{electrons : } E_F = 21\Delta\omega_G + 75 \text{ [cm}^{-1}\text{]}$$

$$\text{holes : } E_F = -18\Delta\omega_G - 83 \text{ [cm}^{-1}\text{]}$$

$$n = \left(\frac{E_F}{11.65} \right)^2 \times 10^{10} \text{ [cm}^{-2}\text{]}$$

The surface charge density $\sigma = ne$ was confirmed by independent electrode capacitance measurements³².

VSFG experimental set-up

A regeneratively amplified Ti:sapphire laser system (Coherent Legend Elite Duo; 14 W, 5 kHz) was pumped by an Nd:YLF laser system (Coherent

Evolution; 10 ns, 60 W, 532 nm, 5 kHz) and ‘seeded’ by a femtosecond Ti:sapphire laser system (Coherent Mira; 100 fs, 400 mW, 806 nm, 80 mHz) that was stretched, amplified and split into two paths. In one path, the 806-nm light (8 W) was recompressed by a pair of gratings to 95 fs (measured via a home-built single-shot autocorrelator) and delivered to an optical parametric amplifier (TOPAS-C Light Conversion) and non-collinear difference frequency generator (NDFG Light Conversion) assembly, yielding tunable femtosecond mid-infrared pulses. The other path of light (6 W) was compressed externally and delivered to a 4f-stretcher. At the focal plane of the 4f-stretcher, a narrowband region (806 nm centred, FWHM = 10 cm⁻¹, ~2 ps) was selected spatially using a mechanical slit. The pulsed visible (40 mW, FWHM = 10 cm⁻¹, ~2 ps) and infrared beams (6 mW, 2,500 cm⁻¹ centred, FWHM = 375 cm⁻¹, ~100 fs) co-propagated in the plane of incidence, were focused to 240 μm and 160 μm respectively, and overlapped (spatially and temporally) at the graphene–water interface to generate the VSFG signal. The average powers and incoming angles of the visible and the infrared beams were 40 mW and 6 mW, and 69° and 61° from the surface normal, respectively. The infrared beam path was purged of atmospheric CO₂ via a purge-gas generator (Parker Balston, model 75-62). The polarizations of the visible, infrared and SFG beams were adjusted using half-wave plates (visible: zero-order quartz half-wave plate, 800 nm, CVI Melles Griot; infrared: zero-order CdSe half-wave plate, 1,000–19,000 nm, 5 mm thick, Alphalas; SFG: zero-order quartz half-wave plate, 670 nm, CVI Melles Griot). An analyser (polarizing beamsplitter cube, extinction ratio >500:1) blocked P-polarized SFG signal to eliminate polarization contamination. The SFG signal was focused at the entrance slit of a single-grating monochromator (Princeton Instruments Acton SP2500 monochromator). The signal was dispersed onto a liquid-nitrogen-cooled charged-coupled device (CCD) array detector (Roeper Scientific, Spec-10:100B, 1,340 × 100 pixels). The SFG spectra were relatively background-free, but a small spectrally flat background from dark current was subtracted from the raw SFG spectra, shifting its baseline close to zero. The non-resonant PPP spectrum of GaAs was used to divide out the spectral shape of the infrared pulse from the SFG spectrum of the D₂O–graphene interface. SFG spectra of the D₂O–graphene interface were acquired in 3 min at each applied voltage.

Raman experimental set-up

Raman spectra of the graphene electrode under applied electrochemical potentials were collected with a Renishaw micro-Raman spectrometer. The measurement was conducted using a backscattering geometry with a 50-μW, linearly polarized 532-nm laser beam focused to 1 μm in diameter. The collected Raman scattered light was dispersed onto a CCD array detector by a single-grating monochromator with a spectral resolution of approximately 0.5 cm⁻¹. Voltage-induced shifts in the Raman frequency of the G-band were collected in both two-terminal and three-terminal configurations. In these electrochemical measurements, the graphene electrode was in contact with D₂O (99.9% purity, Cambridge Isotope Laboratories Inc.), and a 40× lens was immersed in a DI-water reservoir above the sample. To protect the lens from electrolyte, a 13-μm-thick Teflon sheet (American Durafilm Inc.) was used to cover the lens³⁸.

Spectral fitting procedure: decomposition of the graphene–D₂O spectra into $\chi_{s,DL}^{(2)}$ (surface) and $\chi_{s,DL}^{(2)}$ (bulk) contributions

Given Shen and Tian’s discovery that the SFG response of subsurface water molecules influenced by the d.c. field of a charged interface is reminiscent of bulk water and is not affected by the application of charge at the interface¹⁰, we used their results to disentangle the surface $\chi^{(2)}$ response of D₂O at the graphene interface through the following spectral fitting procedure. Adopting the nomenclature of Shen and Tian, it is useful to define $\chi_{s,DL}^{(2)}$, which is the surface response of the diffuse layer¹⁰:

$$\chi_{s,DL}^{(2)} = \frac{\kappa}{\sqrt{\kappa^2 + \Delta k_z}} e^{i \tan^{-1} \left(\frac{\Delta k_z}{\kappa} \right)} \left(\frac{B_{\chi^{(3)},1}}{\omega - \omega_{\chi^{(3)},1} + i\Gamma_{\chi^{(3)},1}} + \frac{B_{\chi^{(3)},2}}{\omega - \omega_{\chi^{(3)},2} + i\Gamma_{\chi^{(3)},2}} \right) e^{i\varphi_{\chi^{(3)}}} \Phi(0)$$

Our fits include Geiger’s formalism of absorptive/dispersive mixing and are based on his readily accessible Mathematica code of three coupled oscillators¹⁸. The extent of mixing depends purely on experimental parameters: refractive indices, incoming beam angles and ionic strength. The refractive index of D₂O in the infrared region of interest was obtained from a publication by Williams et al.⁴², and the ionic strength is that of pure water. The following equation was used to fit our data:

$$I_{SFG} = \left| A_{NR} e^{i\varphi_{NR}} + \frac{B_{\chi^{(2)},1}}{\omega - \omega_{\chi^{(2)},1} + i\Gamma_{\chi^{(2)},1}} e^{i\varphi_{\chi^{(2)},1}} + \frac{B_{\chi^{(2)},2}}{\omega - \omega_{\chi^{(2)},2} + i\Gamma_{\chi^{(2)},2}} e^{i\varphi_{\chi^{(2)},2}} + \frac{B_{\chi^{(2)},3}}{\omega - \omega_{\chi^{(2)},3} + i\Gamma_{\chi^{(2)},3}} e^{i\varphi_{\chi^{(2)},3}} + m \frac{\kappa}{\sqrt{\kappa^2 + \Delta k_z}} e^{i \tan^{-1} \left(\frac{\Delta k_z}{\kappa} \right)} \left(\frac{B_{\chi^{(3)},1}}{\omega - \omega_{\chi^{(3)},1} + i\Gamma_{\chi^{(3)},1}} + \frac{B_{\chi^{(3)},2}}{\omega - \omega_{\chi^{(3)},2} + i\Gamma_{\chi^{(3)},2}} \right) e^{i\varphi_{\chi^{(3)}}} \Phi(0) \right|^2$$

where κ is the inverse Debye length, Δk_z is the inverse coherence length, $\Phi(0)$ refers to the voltage we applied relative to the voltage at which graphene is neutral (graphene is neutral at about 0.1 V versus Ag/AgCl, Fig. 1), B_i/Γ_i is the amplitude, Γ_i is the half-width at half-maximum, ω_i is the central frequency and φ_i is the phase of the i th Lorentzian. Note that our fitting equation differs slightly from what is found in Geiger’s Mathematica code¹⁸: ours includes a non-resonant response, the phases of the two $\chi^{(3)}$ Lorentzians are not independent, and we have included a ‘scaling factor’ m . In our fits, the $\chi^{(3)}$ Lorentzian parameters (B_i , Γ_i and ω_i) were frozen in accordance with estimates made by Geiger, which originates from Tian and Shen’s experimental $\chi_B^{(3)}$ component^{10,18}. Essentially, the strategy to disentangle the surface $\chi^{(2)}$ contribution was to freeze all the known parameters and allow the $\chi^{(2)}$ parameters to float such that our spectra were fitted. Since the central frequencies were given for the OH stretch and not the OD stretch, they were scaled by assuming that the force constants for OH and OD are the same. To be consistent with the literature, the free-OD peak was forced to be positive by restricting and locking its amplitude and phase, respectively. The phases of the two $\chi^{(2)}$ hydrogen-bonded OD stretch peaks were restricted to ± 0.2 radians from the phase at which they were purely absorptive in the imaginary spectrum, since lineshapes that are purely absorptive are simpler to interpret. The phase, $\varphi_{\chi^{(3)}}$, was allowed to float freely in the fit of the 1.0-V spectrum, and its post-fit value was frozen in subsequent fits. The 1.0-V SFG spectrum was fitted first because its hydrogen-bonded peaks were relatively pronounced, and it tended to yield consistent results with respect to changing of the initial guesses of the floating parameters. Qualitatively, our $\chi^{(3)}$ component is consistent with the literature^{9,10,39}: its spectral shape is ‘bulk-like’, and its amplitude is positive for positive fields and negative for negative fields. The scaling factor m effectively served to scale Shen and Tian’s $\chi_{s,DL}^{(2)}$ spectra to our arbitrary scale. Assuming that the $\chi_{s,DL}^{(2)}/\chi_s^{(2)}$ ratio in our spectra should be comparable to Tian and Shen’s, and by also considering the differences in our charge densities, we estimated m to be about 30. We found that our choice in m yielded $\chi_s^{(2)}$ responses that were reasonable. We assessed whether our fits were sensible in the following ways: (1) the $\chi_s^{(2)}$ spectra should be flat on the blue side of the free-OD peak; (2) $\chi_{s,DL}^{(2)}$ should not interfere with the free-OD

peak to a significant extent; (3) the goodness of the fit; (4) through comparison with a theoretical study carried out by Morita et al.³⁹ wherein the surface response increases in intensity as the field is increasingly made negative, and at positive fields the hydrogen-bonded $\chi_s^{(2)}$ and $\chi_{s,DL}^{(2)}$ components interfere destructively. The decomposition into surface and bulk contributions, as well as the fit to the SFG spectra (each plotted with respect to the applied electric field), is shown in Extended Data Fig. 6. The fitting parameter results are shown in Extended Data Table 1.

Data availability

The data that support the findings of this study are available from the corresponding author upon reasonable request.

31. Kim, S. M. et al. The effect of copper pre-cleaning on graphene synthesis. *Nanotechnology* **24**, 365602 (2013).
32. Shi, H. et al. Sensing local pH and ion concentration at graphene electrode surfaces using in situ Raman spectroscopy. *Nanoscale* **10**, 2398–2403 (2018).
33. Chen, C.-C., Chang, C.-C., Li, Z., Levi, A. F. J. & Cronin, S. B. Gate tunable graphene–silicon ohmic/Schottky contacts. *Appl. Phys. Lett.* **101**, 223113 (2012).
34. Stiopkin, I. V., Jayathilake, H. D., Weeraman, C. & Benderskii, A. V. Temporal effects on spectroscopic line shapes, resolution, and sensitivity of the broad-band sum frequency generation. *J. Chem. Phys.* **132**, 234503 (2010).
35. Reina, A. et al. Large area, few-layer graphene films on arbitrary substrates by chemical vapor deposition. *Nano Lett.* **9**, 30–35 (2009).

36. Das Sarma, S., Adam, S., Hwang, E. H. & Rossi, E. Electronic transport in two-dimensional graphene. *Rev. Mod. Phys.* **83**, 407–470 (2011).
37. Froehlicher, G. & Berciaud, S. Raman spectroscopy of electrochemically gated graphene transistors: geometrical capacitance, electron–phonon, electron–electron, and electron–defect scattering. *Phys. Rev. B* **91**, 205413 (2015).
38. Shi, H. et al. Monitoring local electric fields at electrode surfaces using surface enhanced Raman scattering-based Stark-shift spectroscopy during hydrogen evolution reactions. *ACS Appl. Mater. Interfaces* **10**, 33678–33683 (2018).
39. Joutsuka, T., Hirano, T., Sprik, M. & Morita, A. Effects of third-order susceptibility in sum frequency generation spectra: a molecular dynamics study in liquid water. *Phys. Chem. Chem. Phys.* **20**, 3040–3053 (2018).

Acknowledgements This research was supported by Air Force Office of Scientific Research grant no. FA9550-15-1-0184 and FA9550-19-1-0115 (A.M., C.D., M.M., S.B.C., A.V.B.), Army Research Office award no. W911NF-17-1-0325 (B.Z.), US Department of Energy, Office of Science, Office of Basic Energy Sciences award DE-SC0019322 (B.H.), and National Science Foundation award no. CBET-1512505 (H.S.).

Author contributions H.S., B.H., B.Z. and S.B.C. manufactured graphene electrodes. A.M., H.S., B.H. and S.B.C. performed electrochemical measurements and Raman spectroscopy. A.M., C.D., M.M., D.B. and A.V.B. performed VSFG measurements. A.M., C.D., M.M. and A.V.B. contributed VSFG spectral analysis.

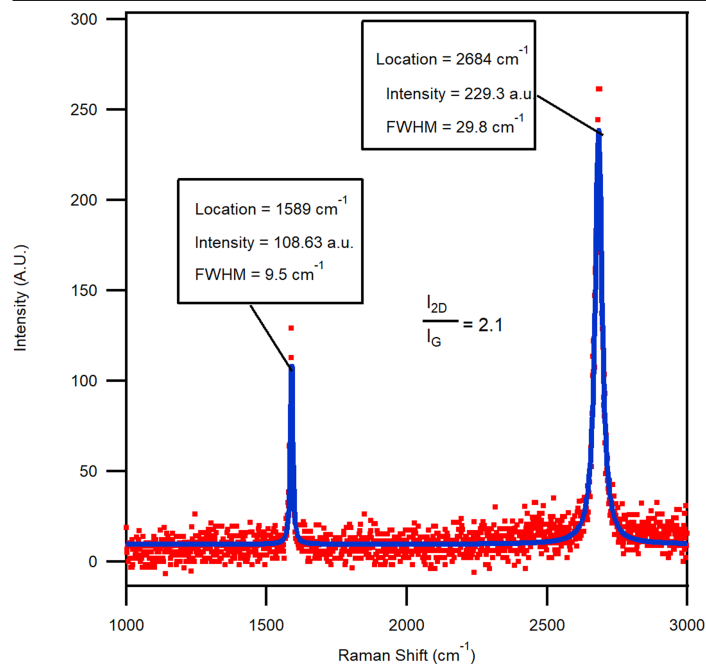
Competing interests The authors declare no competing interests.

Additional information

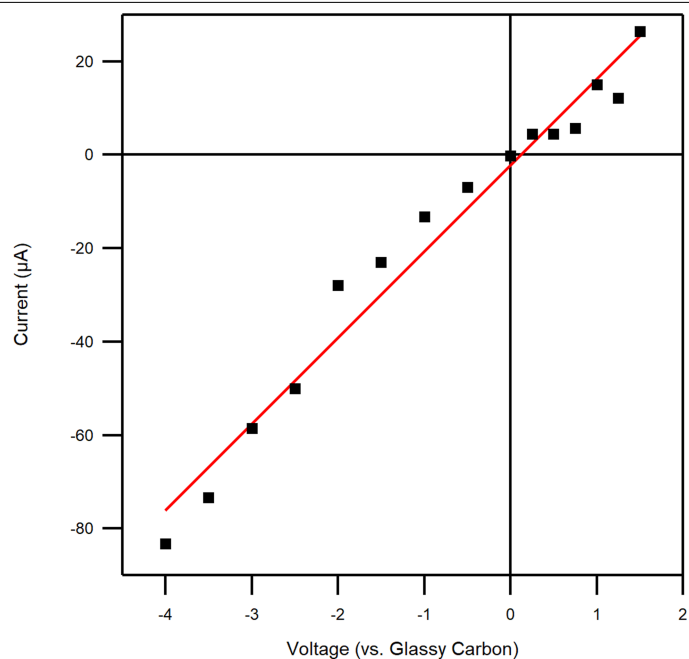
Correspondence and requests for materials should be addressed to A.V.B.

Peer review information *Nature* thanks Franz Geiger, Dusan Bratko, Poul Petersen and the other, anonymous, reviewer(s) for their contribution to the peer review of this work.

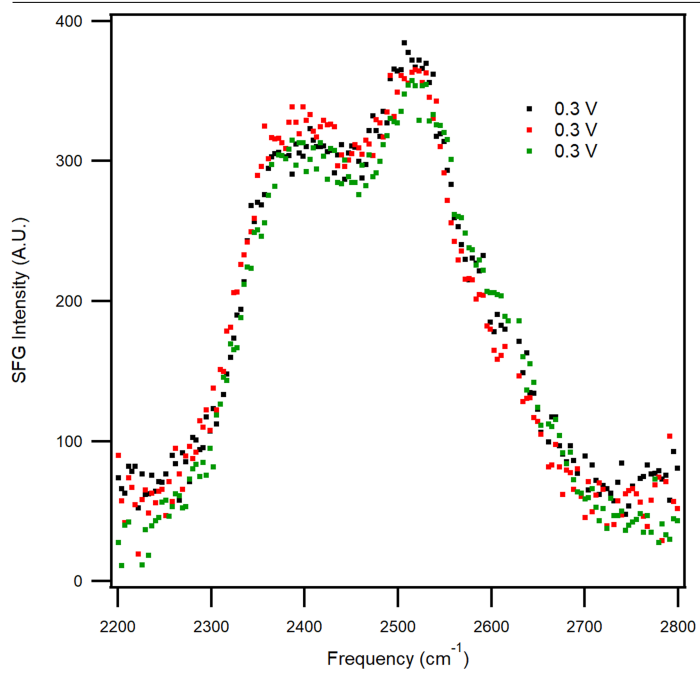
Reprints and permissions information is available at <http://www.nature.com/reprints>.



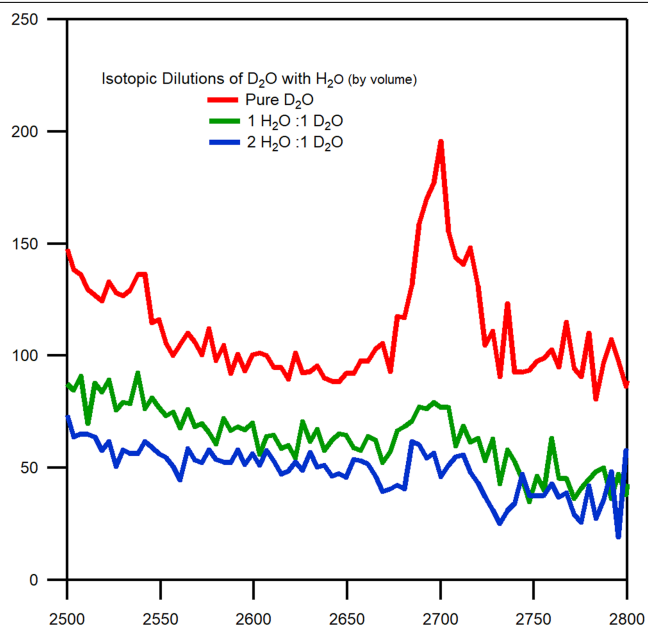
Extended Data Fig. 1 | Raman spectrum of the graphene electrode. For a high-quality, defect-free graphene monolayer, the ratio of intensities of the 2D to G band is about 2.



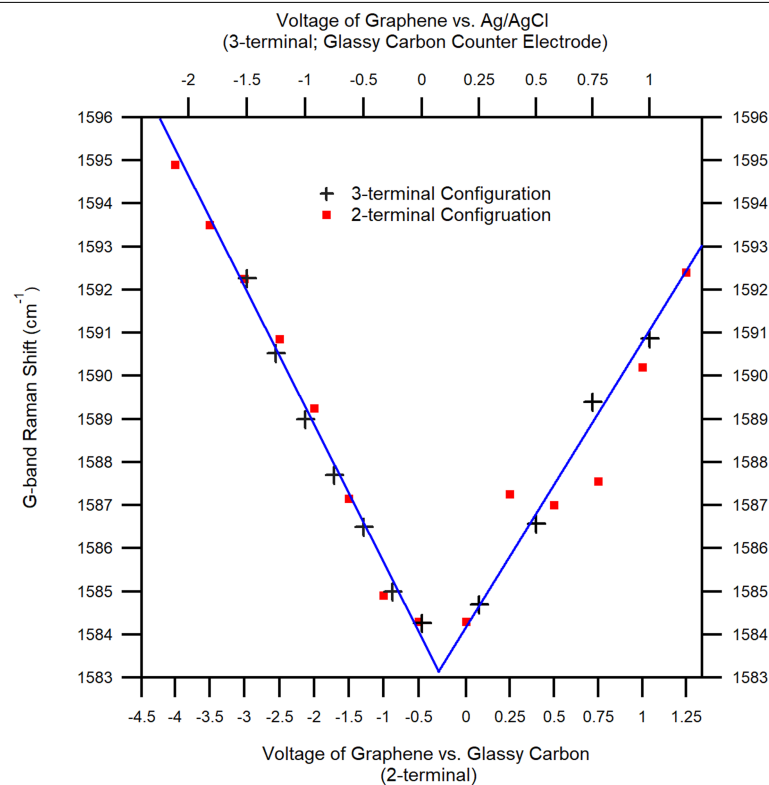
Extended Data Fig. 2 | Electrochemical current with D₂O in the cell versus applied voltage to the graphene electrode versus Ag/AgCl. That the current magnitude does not exceed 100 μA for the voltages that were applied, water splitting does not occur to an appreciable degree.



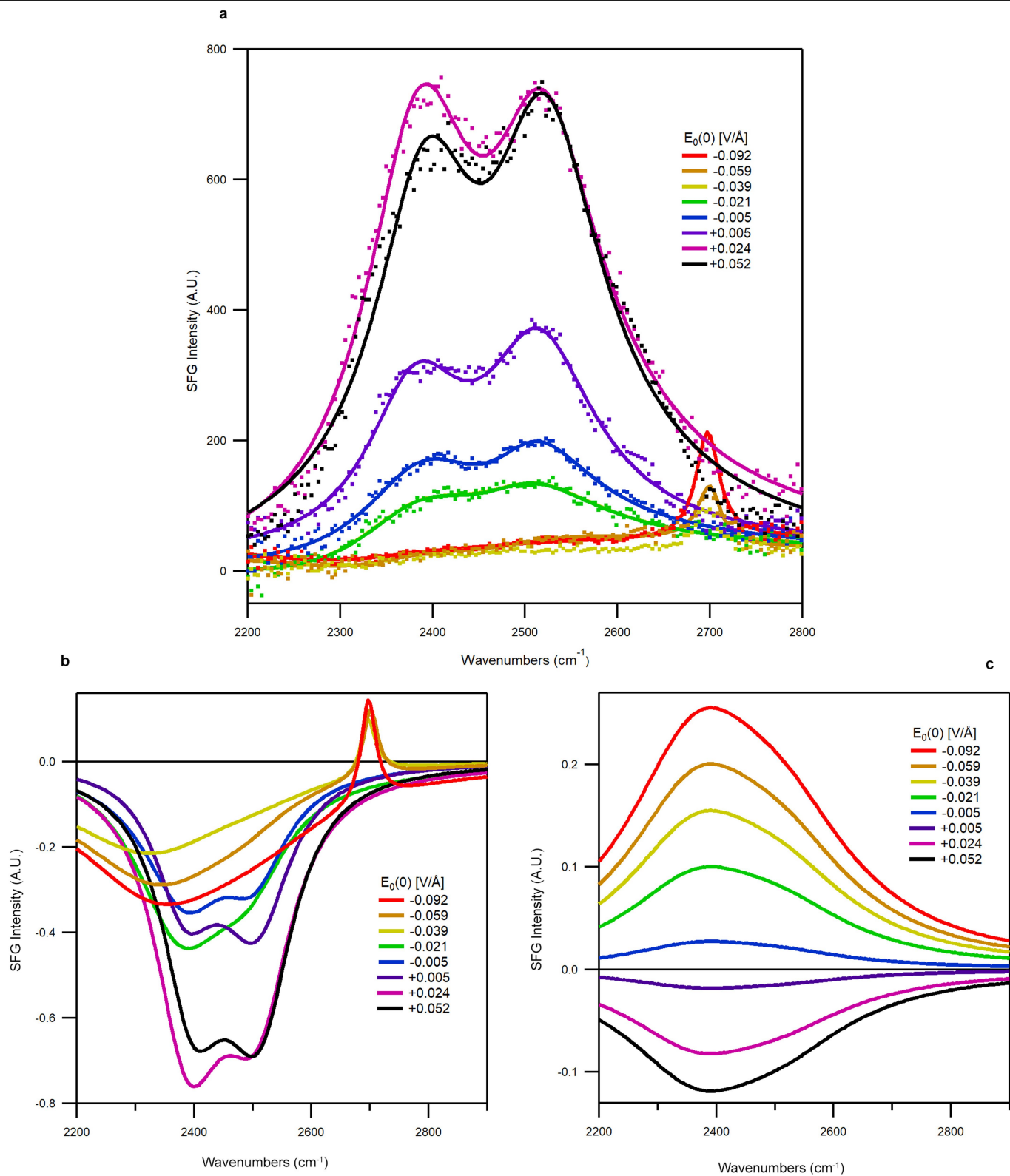
Extended Data Fig. 3 | SFG spectra of the graphene-D₂O interface at 0.3 V (versus Ag/AgCl). Spectra at 0.3 V were taken several times throughout the experiment to verify that there was no drift in the SFG signal with time.



Extended Data Fig. 4 | SFG spectra of graphene-D₂O following dilution with H₂O. Isotopic exchange weakens the peak at $\sim 2,700\text{ cm}^{-1}$, confirming that D₂O is responsible for this signal.



Extended Data Fig. 5 | Linear dependence of G-band Raman shift on applied voltage in both the two-terminal and three-terminal configurations. A two-terminal voltage (applied versus glassy carbon) can be converted to a voltage versus Ag/Cl in the three-terminal configuration by exploiting the linearity of the G-band shift with respect to the applied voltage.



Extended Data Fig. 6 | Electric-field-dependent SFG spectra of the graphene-D₂O interface and its decomposition into $\chi_s^{(2)}$ (surface) and $\chi_{s,DL}^{(2)}$ (bulk) contributions. With the bulk contribution known from the literature, the surface contribution is found through a spectral fitting procedure.

Extended Data Table 1 | Spectral best-fit results for the decomposition of $\chi^{(2)}$ and $\chi^{(3)}$ responses

	$E_0(0)$ (V/Å)	+0.092	+0.059	+0.039	+0.021	+0.005	-0.005	-0.024	-0.052
$\chi^{(2)}$	ω_1	2340.0	2351.9	2333.9	2369.0	2385.4	2378.8	2384.0	2392.5
	ω_2	2496.7	2486.1	2513.3	2496.9	2502.1	2511.9	2512.9	2516.3
	ω_3	2697.2	2701.1	2694.5	0.0	0.0	0.0	0.0	0.0
	Amplitude ₁	-0.27	-0.27	-0.20	-0.36	-0.30	-0.29	-0.59	-0.48
	Amplitude ₂	-0.12	-0.06	-0.04	-0.18	-0.21	-0.34	-0.48	-0.53
	Amplitude ₃	0.24	0.16	0.13	0	0	0	0	0
	B ₁	-47.33	-46.47	-34.77	-35.63	-25.84	-18.75	-42.56	-32.20
	B ₂	-20.52	-5.69	-5.63	-14.72	-14.54	-24.27	-35.30	-38.06
	B ₃	3.66	2.40	1.98	0.00	0.00	0.00	0.00	0.00
	Γ_1	175.0	171.3	175.0	98.1	86.8	64.3	71.9	66.6
	Γ_2	175.0	97.9	134.8	83.2	68.6	71.7	73.2	72.0
	Γ_3	15.3	15.0	14.9	0.0	0.0	0.0	0.0	0.0
	ϕ_1	3.22	3.34	3.34	2.94	3.19	2.90	2.94	2.94
	ϕ_2	3.11	3.23	3.34	3.34	3.15	3.34	3.34	3.34
	ϕ_3	3.14	3.14	2.94	3.14	0.00	0.00	0.00	0.00
$\chi^{(3)}$	ω_1	2365	2365	2365	2365	2365	2365	2365	2365
	ω_2	2510	2510	2510	2510	2510	2510	2510	2510
	Amplitude ₁	1.33	1.33	1.33	1.33	1.33	1.33	1.33	1.33
	Amplitude ₂	0.67	0.67	0.67	0.67	0.67	0.67	0.67	0.67
	B ₁	200	200	200	200	200	200	200	200
	B ₂	100	100	100	100	100	100	100	100
	Γ_1	150	150	150	150	150	150	150	150
	Γ_2	150	150	150	150	150	150	150	150
	ϕ_1	4.73	4.73	4.73	4.73	4.73	4.73	4.73	4.73
NR	B _{NR}	0.25	0.18	0.16	0.13	0.13	0.15	0.09	0.06
	ϕ_{NR}	1.79	1.52	1.71	0.10	-0.67	-1.21	-0.15	-0.11